

# Tunable microwave dual-band patch antenna through integration of metamaterials and nanoscale ferroelectrics


Martino Aldrigo<sup>1,\*</sup>, Anna C. Tasolamprou<sup>2,3</sup>, Dan Vasilache<sup>1</sup>, Maria Kafesaki<sup>2,4</sup>,  
Sergiu Iordanescu<sup>1</sup>, Florin Nastase<sup>1</sup>, and Mircea Dragoman<sup>1</sup>

<sup>1</sup>*National Institute for Research and Development in Microtechnologies (IMT-Bucharest), 126A Erou Iancu Nicolae Street, Voluntari, Ilfov 077190, Romania*

<sup>2</sup>*Institute of Electronic Structure and Laser, Foundation for Research and Technology Hellas, N. Plastira 100, Heraklion, Crete 70013, Greece*

<sup>3</sup>*Department of Physics, National and Kapodistrian University of Athens, Athens 15784, Greece*

<sup>4</sup>*Department of Materials Science and Technology, University of Crete, Heraklion, Crete, Greece*

 (Received 3 February 2023; revised 8 September 2023; accepted 25 September 2023; published 25 October 2023)

We present a CMOS-compatible silicon-based patch antenna providing a tunable dual-band behavior in the 8–12 GHz frequency range. The dual-band operation is induced by an asymmetrically aligned complementary split-ring resonator (CSRR) meta-atom, etched in the metallic, back-reflector part of the antenna. By rotating and moving the CSRR we can force a multimode response in the antenna cavity, which leads to the excitation of two highly radiating modes at 8 and at 10.35 GHz. The tunability is provided by the inclusion of a planar phase shifter based on an ultrathin hafnium oxide ferroelectric layer interposed between the silicon substrate and the top metallization, thus allowing us to electrically modify the radiation characteristics of the antenna in terms of resonant frequency, amplitude of the reflection coefficient, and gain, with sub- $\mu$ s values of the polarization switching time. The results are supported by theoretical modeling, full-wave electromagnetic simulations, fabrication, and experimental validation and represent a stimulus for the integration of metamaterials and two-dimensional ferroelectrics into high-frequency electronics.

DOI: [10.1103/PhysRevApplied.20.044067](https://doi.org/10.1103/PhysRevApplied.20.044067)

## I. INTRODUCTION

Metamaterials and metamaterial-based devices and components have been gaining increasing interest in recent years, thanks to the possibility of manipulating electromagnetic (EM) waves by creating artificial dielectric and magnetic materials with customized properties, i.e., electric permittivity and magnetic permeability. Metamaterials and their two-dimensional (2D) analogue, metasurfaces, provide access to exotic EM properties, not found in natural materials, which is achieved by properly engineering their subwavelength elementary building blocks, i.e., the so-called meta-atoms. Due to the meta-atoms' architecture the local currents excited by an impinging EM wave are engineered, thus offering the possibility of unconventional EM wave control, which leads to a variety of applications in the vast EM spectrum, from sensing, shielding, energy harvesting, to wave-front shaping and beam steering [1–3]. The integration of tunable and active materials enables even more advanced EM functionalities and external control. Depending on the frequency regime these

materials may be, for example, electric elements [4], 2D materials for ultrafast modulation [5], liquid crystals, gyrotropic elements, and many others [6] that further provide enhanced and ultrafast modulation techniques. Within this landscape of vast possibilities, metasurface-based applications related to emerging wireless communication technologies [7–9] have been gaining growing attention.

In the current panorama of wireless communications (5G and the future 6G), the spectrum allocation assigns specific frequency ranges to different applications, one of the most important ones being the so-called *X* band (i.e., 8.2–12.4 GHz), which is intensively exploited for space communications, radar systems, and terrestrial links. For all the latter usages, an agile *front end* with reconfigurable multiband characteristics is a highly desirable target, not always easily achievable unless a multidisciplinary approach is adopted, which in turn could translate into an unbearable technological complexity. Furthermore, a key aspect is the development of processes that are CMOS compatible, as this ensures a large-scale fabrication for high-volume commercialization. Hence, the design, fabrication, and experimental characterization of silicon

\*martino.aldrigo@gmail.com

(Si)-based devices and components becomes compelling. Metamaterials can be profitably exploited in antennas [10], for example, for miniaturization purposes [11,12], to increase the radiation, gain and the aperture efficiency [13, 14], in EM band-gap (EMBG) structures to enhance the isolation in arrays [15], and for high-impedance surface-based leaky-wave antennas [16], just to name a few. The mostly recent works report dual- or even multiband antennas integrating metamaterials up to 28 GHz [17–24], and dual-band metasurface-based filters [25]. However, the cited state of the art is based on epoxy FR4 substrates, PTFE composites, and laminates, with no CMOS compatibility characteristics, thus hindering their monolithic integration with Si.

The automated control desired for the vast majority of contemporary wireless communications comes hand in hand with antenna reconfigurability. When speaking about reconfigurable metamaterial-based antennas for actual applications, things become even more complicated in terms of design and efficiency. Tunability may be achieved using varactors [4,26] or *p-i-n* diodes, and FETs [27] that generally provide high tunability and feasible integration but for which, at the same time, the power consumption is not negligible for real-time applications. Efficient modulators have been proposed in graphene-based metasurfaces for near- and midinfrared applications [28], and multiwideband THz communications [29], which provides high and ultrafast modulation but is more challenging in terms of integration and local control. Other approaches may include mechanical tuning of chiral metamaterial antennas based on three-dimensional helices [30], thermal and magnetic structures, and more [31].

In this work, we propose a simple yet effective solution to obtain a tunable dual-band behavior in the *X* band enabled by the integration of an ultrathin, essentially 2D, ferroelectric layer with ultrafast response controlled by the application of an external electric field (Fig. 1).

This ferroelectric layer is interposed between the Si substrate and the top metallization, and is the key element of an interdigitated capacitor with variable capacitance (varactor) that confers low-voltage tunability to the metamaterial antenna. For the dual-band operation, we combine a patch antenna with a complementary split-ring resonator (CSRR) etched in the back metal reflector and placed in an asymmetric fashion with respect to the antenna itself. The substrate consists of a standard high-resistivity Si (HRSi) layer, on top of which a nanometer-thick layer of ferroelectric zirconium-doped hafnium oxide (HZO) is deposited via thermal atomic layer deposition (ALD). The presented antenna has a dual-band behavior within the *X* band and, what is more, its matching and radiation characteristics can be continuously tuned via the application of a small in-plane dc bias voltage (i.e.,  $\pm 2$  V) onto the ultrathin HZO film with sub- $\mu$ s values of the polarization switching time.

The paper is organized as follows: first, we present the theoretical investigation of the response of the CSRR and the inclusion of the CSRR in the ground plane of the patch antenna, which induces a multimode response of the patch antenna. Then, we provide the complete EM, numerically optimized design and simulation of the performance of the tunable dual-band antenna. The last section of the paper is dedicated to the experimental validation of the hypothesis by means of thorough measurements of the reflection coefficient and transmission characteristics of the antenna, under different values of the dc bias voltage applied to the HZO thin film.

## II. MULTIMODE CAVITY RESPONSE

In this section we present an analysis of the resonant response of the antenna cavity. In this initial approximation we perform an estimation and analysis of the cavity resonance by calculating its scattering parameters and in particular the reflectivity. The metal-insulator-metal type

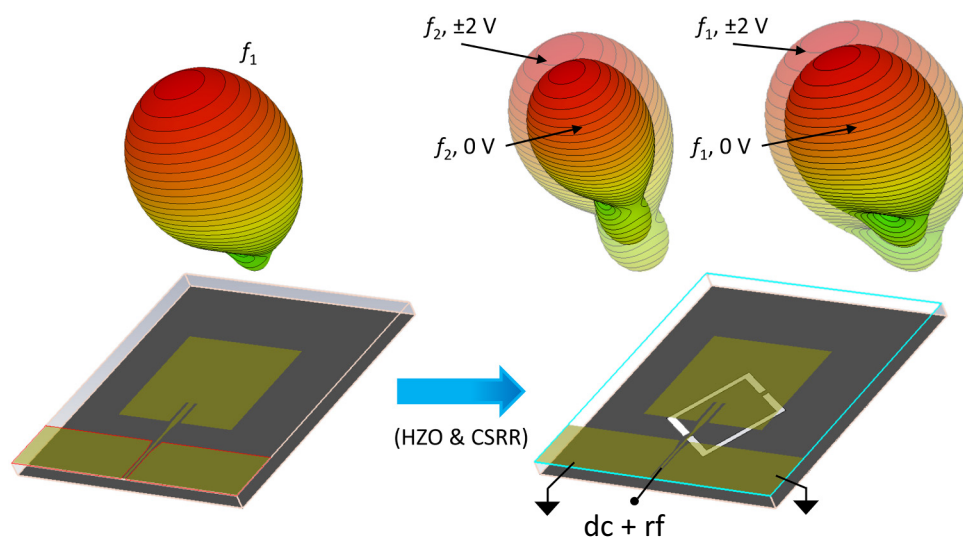


FIG. 1. Proposed concept of ferroelectric-based dual-band metamaterial antenna with tunable characteristics. The radiation patterns correspond to the structures and frequencies shown in Figs. 3 and 4.

cavity is created by the combination of two kinds of metallic resonators at the termination of the cavity. The rectangular patch is placed on the top of the cavity, whereas at the bottom of the cavity we have the infinite back reflector where the CSRR is imprinted. To obtain a better insight of the multiband response, we start with the analysis of the sole CSRR in a standalone form, i.e., the structure placed on an infinite dielectric substrate. The split-ring resonator is the most standard scheme of designing the local resonator in a meta-atom. It consists of, most commonly, a metallic loop with one or more gaps [32,33] and enabled fascinating artificial electromagnetic features, from optical magnetism to enhanced chirality [34,35]. When an EM wave of proper polarization, frequency, and direction of propagation impinges the SRR-based metamaterial-metasurface, alternating currents are excited along the elements while charge is accumulated in the adjacent elements providing the controllable magnetic and electric response. In all, the SRR behaves as an  $LC$  circuit with the resonance being a function of the shape of the ring, the size and position of the gaps, and the details of the impinging wave. In the CSRR, according to Babinet's principle, the transmission and reflection behavior as well as the scattered electric and magnetic fields are interchanged [36–38]. The top view of the CSRR under consideration is schematically shown in Fig. 2(a). It consists of a metallic layer [gray color in Fig. 2(a)] where the SRR is etched [the blue color in Fig. 2(a) corresponds to the dielectric substrate]. The size of the unit cell is  $4.5 \times 4.5 \text{ mm}^2$ , the width of the etched regions is 0.25 mm and the size of the gaps is 0.25 mm. To facilitate the calculations, we assume a periodic structure large enough so that the neighbor coupling is minimal. The numerical analysis is performed with the use of the full wave, commercially available solver, COMSOL Multiphysics. In the schematic we show the two limiting cases of the unit rotational alignment, i.e., the  $0^\circ$  rotation (bottom panel), with the metallic gaps placed in the horizontal direction, and the  $90^\circ$  rotation (upper panel), with the metallic gaps placed in the vertical direction. In this standalone CSRR we investigate the scattering response, i.e., the reflectivity for various rotation angles in the range  $[0-90]^\circ$  and in the normalized frequency range  $[0.2-0.7] a/\lambda$ , assuming a plane wave of  $E_y$  polarization impinging normally to the structure (notice that due to the symmetry the  $E_y$  polarization response in the  $90^\circ$ -rotated CSRR case is the same as the response of the  $0^\circ$  rotation in the  $E_x$  polarization). The results are shown in Fig. 2(b). The white areas correspond to zero dB (i.e., full) reflection and stand far from the cavity's resonant modes. The resonant modes, appearing as reflection minima, are marked with the dark red and black areas in Fig. 2(b). Looking at the limiting cases, when the rotation angle is  $0^\circ$  and  $90^\circ$ , we observe that the structure exhibits single resonances at lower and higher frequencies, respectively, with the locally excited field presented in Fig. 2(c)

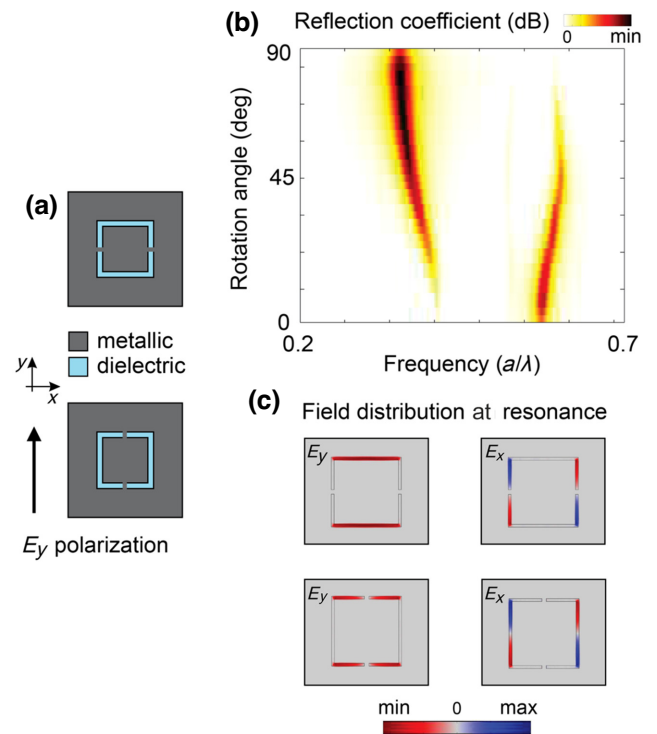


FIG. 2. (a) The complementary SRR under consideration placed on top of a dielectric substrate (may be equivalently considered as free standing); (b) reflection coefficient spectra of the free-standing CSRR, under the assumption of  $E_y$  polarization, for different rotation angles in the range  $0^\circ-90^\circ$  ( $y$  axis) and in the normalized frequency range  $[0.2-0.7] a/\lambda$  ( $x$  axis); (c) distribution of the locally excited EM field at resonance for rotation angle  $0^\circ$  (bottom panel) and  $90^\circ$  (top panel).

(bottom and upper panel, respectively). As expected, the field is concentrated in the etched dielectric spacer between the metallic sides. For the  $0^\circ$  rotation angle case the  $E_y$  field is concentrated in the dielectric region on the CSRR sides bearing the metallic gap that does not include metallic gaps (area equal with the unit size). Figure 2(b) shows that, for intermediary values of the rotation angle within the considered range, we have the coexistence of a form of both resonances (found alone in the limiting cases). In other words, in this case a multimode response appears, which is one of the origins of the multimode response of the antenna cavity. The in-depth investigation of cavity's response without and with the CSRR can be found in Appendix A.

### III. ELECTROMAGNETIC DESIGN AND SIMULATION OF THE MICROWAVE PATCH ANTENNA INTEGRATING A BACKSIDE COMPLEMENTARY SPLIT-RING RESONATOR

#### A. Patch antenna design and simulations

After the study of the asymmetric CSRR-induced multimode response, we performed thorough EM simulations

and rigorous numerical optimization of the design of the complete metamaterial-based patch antenna by using CST Microwave Studio, a three-dimensional (3D) full-wave EM solver widely used for the design of complex EM structures.

In Fig. 3(a), the top view of the proposed solution is shown: it is a rectangular patch antenna with length  $L = 4.1$  mm and width  $W = 5$  mm (since  $W > L$  ensures an increase of antenna's directivity), whereas the HZO/HRSi substrate has dimensions  $L_{\text{sub}} = W_{\text{sub}} = 10$  mm. The patch antenna is integrated with a coplanar waveguide (CPW)-to-microstrip transition, as it is a necessary prerequisite to perform fast on-wafer measurements without the need of external connectors and cables. In fact, using standard CPW probe tips of the ground-signal-ground (GSG) type, it is possible to directly contact the measuring instruments to the excitation port ["rf input" in Fig. 3(a)] of the antenna under test (AUT). At the end of the CPW section, a tapered geometry allows a smooth transition to the microstrip, thus preserving the matching to the characteristic impedance of

the excitation port (i.e.,  $50 \Omega$ , which is a typical value for calibrated microwave systems). Finally, the optimal impedance matching to the patch is realized by means of a so-called "inset" [see Fig. 3(a)]: the microstrip line is connected to the antenna in a precise point (by EM optimization) along the  $y$  axis, since the impedance of the patch varies between  $\infty$  (open circuit) at the lower margin and  $0$  (short circuit) in the center.

According to Fig. 3(b), the main dimensions of the CSRR etched on the back reflector are  $L_{\text{CSRR}} = 3.1$  mm,  $W_{\text{CSRR}} = 0.25$  mm, and  $G_{\text{CSRR}} = 0.25$  mm, whereas the rotation angle (with respect to the  $x$  axis) is equal to  $60^\circ$ . Also, there is an offset of about 1.48 mm between the center of the patch and the center of the CSRR, meaning that the CSRR is located below the lower aperture of the antenna (i.e., between the CPW section and the patch). Size and position of the CSRR are the result of a computational optimization based on the results of the previous section, and they guarantee the multimode response that generates the second resonance. Finally, Fig. 3(c) shows the cross section of the AUT, in which the top metallization is gold (Au) and the back metallization is aluminum (Al), with  $t_{\text{Au}} = t_{\text{Al}} = 500$  nm, whereas  $t_{\text{HZO}} = 7$  nm and  $t_{\text{HRSi}} = 525 \mu\text{m}$ .

Figure 4 shows the main results obtained from the 3D EM simulations. First, one can notice from Fig. 4(a) (left vertical axis) that the reflection coefficient  $|S_{11}|$  of the patch antenna without CSRR (solid blue curve) has a single resonance at 10 GHz, whereas the presence of the CSRR (solid red curve) generates a second resonance at 8 GHz and slightly shifts upwards the dominant mode, from 10 to 10.35 GHz. In all cases,  $|S_{11}|$  refers to a normalization impedance of  $50 \Omega$  and is better than  $-15$  dB. Figure 4(a) presents the imaginary part of the input impedance on the right vertical axis, which has one zero without CSRR and two zeros with CSRR, at the same frequencies of the  $|S_{11}|$  minima, as expected. Then, Fig. 4(b) displays the total efficiency  $\eta_{\text{tot}}$  without CSRR (solid blue curve) and with CSRR (solid red curve) as a function of frequency.  $\eta_{\text{tot}}$  is defined as follows:

$$\eta_{\text{tot}} = \frac{P_{\text{rad}}}{P_{\text{stim}}}, \quad (1)$$

where  $P_{\text{rad}}$  is the radiated power (in  $W$ ) and  $P_{\text{stim}}$  is the stimulated power (in  $W$ ), which is calculated from the power that is delivered by the signal generator to the port. Hence,  $\eta_{\text{tot}}$  also considers the losses due to reflection at the feeding location and, for this reason, is a much more comprehensive measure of the antenna's efficiency. From Fig. 4(b) it is apparent that the patch antenna without CSRR has its efficiency peak of about 52% at 10 GHz (gain of about 2.2 dBi), while introducing the CSRR produces an upshift at 10.35 GHz with a peak value of about 73% (gain of about 3.6 dBi) and an alternative peak at 8 GHz,

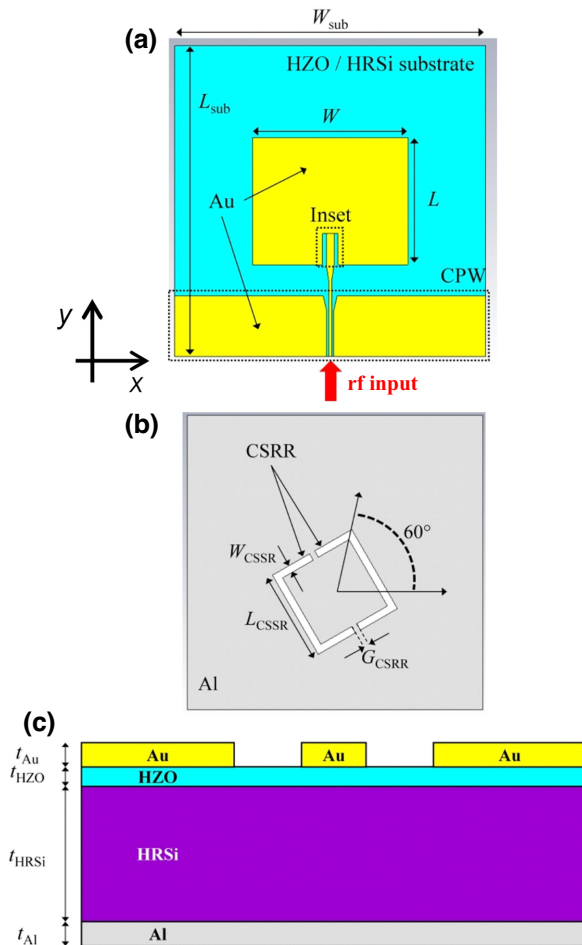


FIG. 3. 3D EM layout of the patch antenna with (a) top, (b) back, and (c) cross-section view. The main materials and dimensions are also provided.

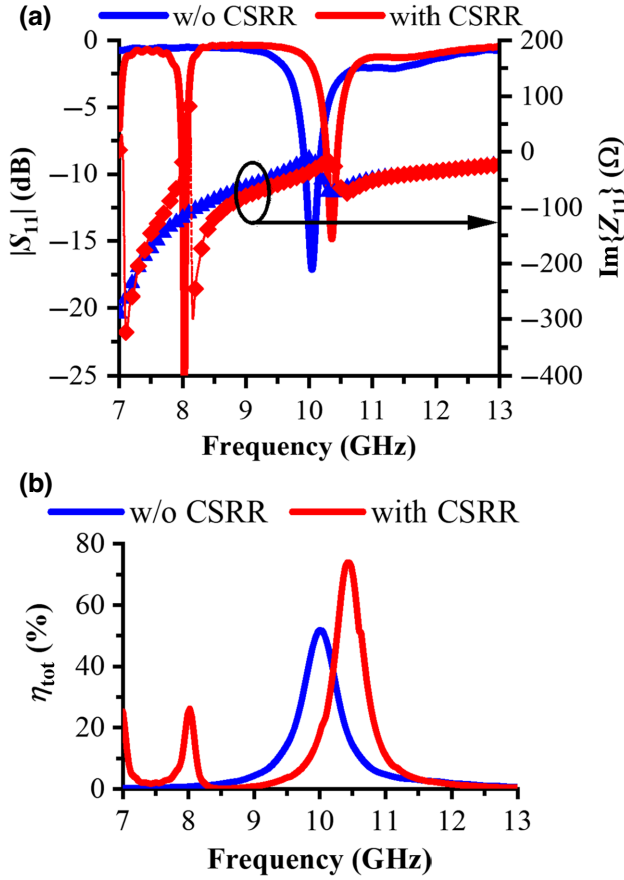


FIG. 4. EM simulations of the patch antenna without and with the back CSRR, in terms of (a)  $|S_{11}|$  (dB) and  $\text{Im}\{Z_{11}\}$  ( $\Omega$ ), and (b) total efficiency  $\eta_{\text{tot}}$  (%).

with a value of about 26% (gain of about  $-1.6$  dBi). We can conclude that the presence of the CSRR does not hinder the radiation of the dominant mode and, for reasons that will be explained later when presenting the equivalent circuit model, produces another resonant mode at lower frequency, with a smaller radiation but still useful for a dual-band application.

From the theory, it is known that the EM fields at the edges of a patch undergo fringing effects, which results into electrically longer dimensions. Since the dominant mode is the  $TM_{010}$ , the resonant frequency  $(f_r)_{010}$  is expressed as follows [39]:

$$(f_r)_{010} = \frac{v_0}{2\sqrt{\epsilon_{\text{eff}}L_{\text{eff}}}}, \quad (2a)$$

$$L_{\text{eff}} = L + 2\Delta L, \quad (2b)$$

$$\Delta L = 0.412 h \frac{(\epsilon_{\text{eff}} + 0.3) \left(\frac{W}{h} + 0.264\right)}{(\epsilon_{\text{eff}} - 0.258) \left(\frac{W}{h} + 0.8\right)}, \quad (2c)$$

where  $v_0$  is the free-space speed of light,  $\epsilon_{\text{eff}}$  is the effective permittivity,  $L_{\text{eff}}$  is the effective length of the antenna,  $L$  and

TABLE I. Extracted values of  $\epsilon_{\text{eff}}$  for the proposed patch antenna.

CSRR	Frequency (GHz)	$\epsilon_{\text{eff}}$
No	10	10.942
Yes	8 (first res.)	17.155
Yes	10.35 (second res.)	10.358

$W$  are the length and the width of the antenna as in Fig. 3, and  $h = t_{\text{HRSi}} + t_{\text{HZO}}$ . An analytical expression for  $\epsilon_{\text{eff}}$  is a nontrivial issue, since it must take the ultrathin ferroelectric layer into account, considering that it is deposited directly onto the HRSi bulk substrate. The extraction of  $\epsilon_{\text{eff}}$ , as a function of the applied dc voltage  $V_b$ , can benefit from a mixed theoretical and experimental approach [40]. On the other hand, several attempts have been done to provide the dependence of the ferroelectric permittivity on the electric field based on the modified Johnson model [41,42]. However, in the present case of study  $\epsilon_{\text{eff}}$  is a much more useful quantity, which is also related to the geometry of the analyzed structure. For HZO, its relative permittivity  $\epsilon_r^{\text{HZO}}$  roughly varies between 30 and 60. Using the EM simulated values of the resonant frequencies [see Fig. 4(a)], one can solve the nonlinear system in Eqs. (2a)–(2c) to extract  $\epsilon_{\text{eff}}$ , thus obtaining the results shown in Table I, whereas the average values for  $L_{\text{eff}}$  and  $\Delta L$  are 4.5 and 0.2 mm, respectively. In particular, Table I demonstrates at a glance that the EM effect of the CSRR etched on the back metallization is to provide an artificially increased value of  $\epsilon_{\text{eff}}$  that generates the alternative resonance at 8 GHz and basically preserves the dominant mode. These results are further confirmed by the EM simulated directivity (see Appendix B).

To better understand the manipulation mechanism of the antenna, we present in the following the equivalent circuit of the antenna without and with the CSRR. In detail, a patch antenna can be modeled by means of a parallel  $RLC$  resonator, in which the three circuit components are as follows:

$$R_r = \frac{Q_r}{2\pi f C_{\text{patch}}}, \quad (3a)$$

$$L_{\text{patch}} = \frac{1}{(2\pi f)^2 C_{\text{patch}}}, \quad (3b)$$

$$C_{\text{patch}} = \frac{\epsilon_0 \epsilon_{\text{eff}} W L}{2 t_{\text{sub}}} \cos^{-2} \left( \frac{\pi y_0}{L} \right), \quad (3c)$$

where  $R_r$  is the radiation resistance,  $Q_r$  is the radiation quality factor,  $t_{\text{sub}}$  is substrate's thickness, and  $y_0$  is the distance of the feed point from the edge of the patch.  $R_r$  represents the transfer of energy from the antenna to the free space, while in the circuit model it refers to the input section of the patch.  $C_{\text{patch}}$  is mainly due to the parallel-plate geometry of the cavity, and the term  $\cos^{-2}(\pi y_0/L)$

can be approximated to 1. Finally,  $L_{\text{patch}}$  takes all the inductive effects into account (mostly associated to the metallization of the patch) and gives the resonant frequency of the parallel  $RLC$  resonator. With some manipulations,  $R_r$  and  $Q_r$  can be expressed as follows [39]:

$$R_r = \frac{\omega\epsilon_0}{\sigma_{\text{sub}}} \frac{1}{2\pi f C_{\text{patch}}}, \quad (4a)$$

$$Q_r = R_r \sqrt{\frac{C_{\text{patch}}}{L_{\text{patch}}}}, \quad (4b)$$

where  $\sigma_{\text{sub}}$  is the substrate's conductivity. Hence, knowing the geometry of the antenna and the characteristics of the substrate, one can calculate in sequence  $C_{\text{patch}}$ ,  $L_{\text{patch}}$ , and  $R_r$ , for both cases without and with CSRR. For the latter, the straightforward equivalent circuit comprises two parallel  $RLC$  resonators in cascade, but with different values of the circuit components, which reflect the physical characteristics of the CSRR. The final circuits are shown in Fig. 5(a) (standalone patch) and Fig. 5(b) (patch with the CSRR). In both cases, we have used a 1-port circuit representation, in which the  $RLC$  resonator loading the transmission line-based circuit is connected to ground (which models the back reflector, as it is the reference plane for both the patch antenna and the CSRR). This approach preserves the 1-port nature of the antenna, even

if 2-port equivalent circuits have been widely reported in the literature as well [43–48].

Each circuit element has a specific physical correspondence (like the microstrip feedline, which is modeled through inductors for the metallization and through a capacitor to consider the capacitive effect to ground). Specifically, the  $RLC$  resonators in Figs. 5(a) and 5(b) have the values reported in Table II.

As expected, one can notice that the presence of the CSRR slightly modifies the values of the resonator modeling the patch antenna due to coupling effects of the mode excited by the CSRR with the EM field distribution of the fundamental mode. This reflects into a frequency shift and a small increase of the radiation quality factor. In contrast, the resonator describing the CSRR exhibits an equivalent capacitance which is 65% bigger than that of the first resonance (due to the capacitive nature of the CSRR itself), and the radiation resistance is 50% bigger. In other words, we can predict that at the second resonance (induced by the meta-atom) the antenna will radiate with less efficiency due to a twofold phenomenon, i.e., the power dissipation associated to surface currents of bigger intensity at the edges of the CSRR, and a bigger amount of reactive power coming from the equivalent capacitance of the CSRR [49]. If we compare the EM- and circuit-simulated reflection coefficients, we obtain the results shown in Fig. 6. In particular, Figs. 6(a) and 6(b) refer to the patch antenna

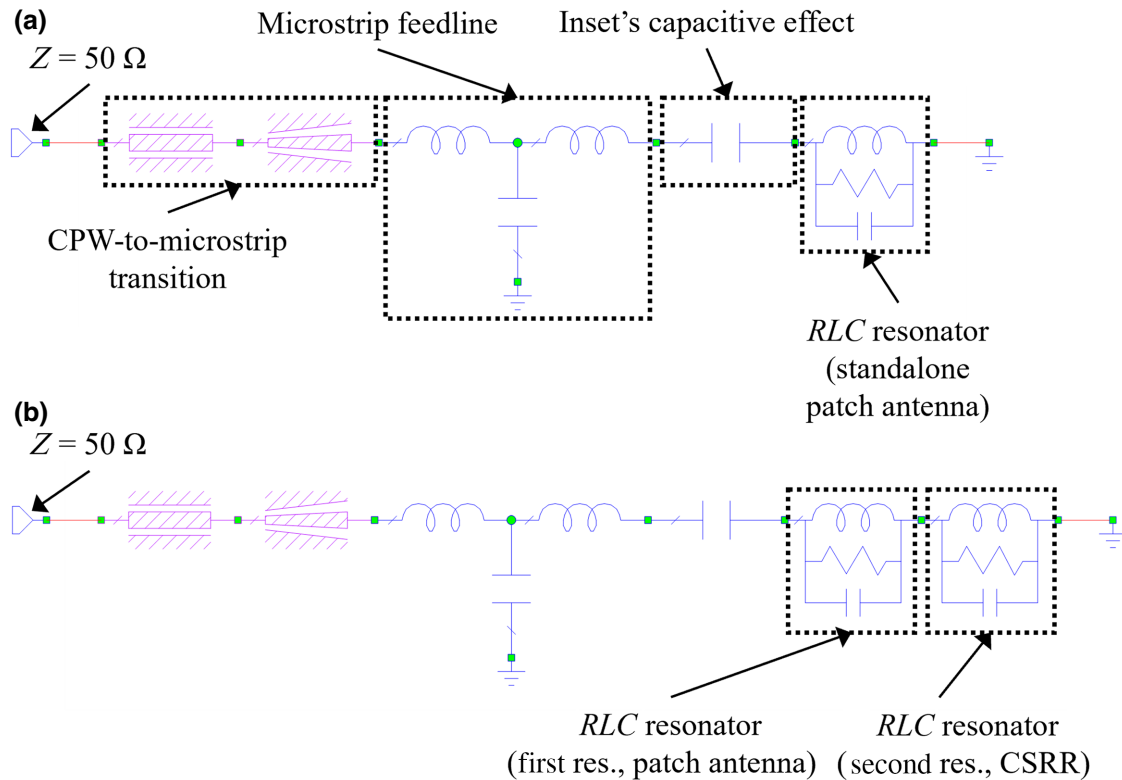


FIG. 5. Equivalent circuit of the (a) standalone patch antenna and (b) patch antenna with CSRR.

TABLE II. Extracted values of the  $RLC$  resonators in Figs. 5(a) and 5(b).

$RLC$ (standalone)	Value	$RLC$ (first res.)	Value	$RLC$ (second res.)	Value
$R_{r,standalone}$	543 $\Omega$	$R_{r,first\ res.}$	588 $\Omega$	$R_{r,second\ res.}$	882 $\Omega$
$L_{standalone}$	0.21 nH	$L_{first\ res.}$	0.2091 nH	$L_{second\ res.}$	0.2091 nH
$C_{standalone}$	1.173 pF	$C_{first\ res.}$	1.11 pF	$C_{second\ res.}$	1.83 pF
$Q_{r,standalone}$	$\approx 40$	$Q_{r,first\ res.}$	$\approx 43$	$Q_{r,second\ res.}$	$\approx 83$

without meta-atom [circuit schematic in Fig. 5(a)] and with meta-atom [circuit schematic in Fig. 5(b)], respectively. The agreement is excellent in both cases.

From Fig. 6(b) one can see that the EM simulations provide one more resonance around 7 GHz. This frequency falls within the  $C$  band (i.e., 4–8 GHz) and, from an experimental point of view, other equipment and a different microwave setup are necessary to perform a thorough far-field characterization. However, a detailed description of the physical phenomenon occurring between 5 and 7 GHz, corroborated by EM simulations, can be found in Appendix C.

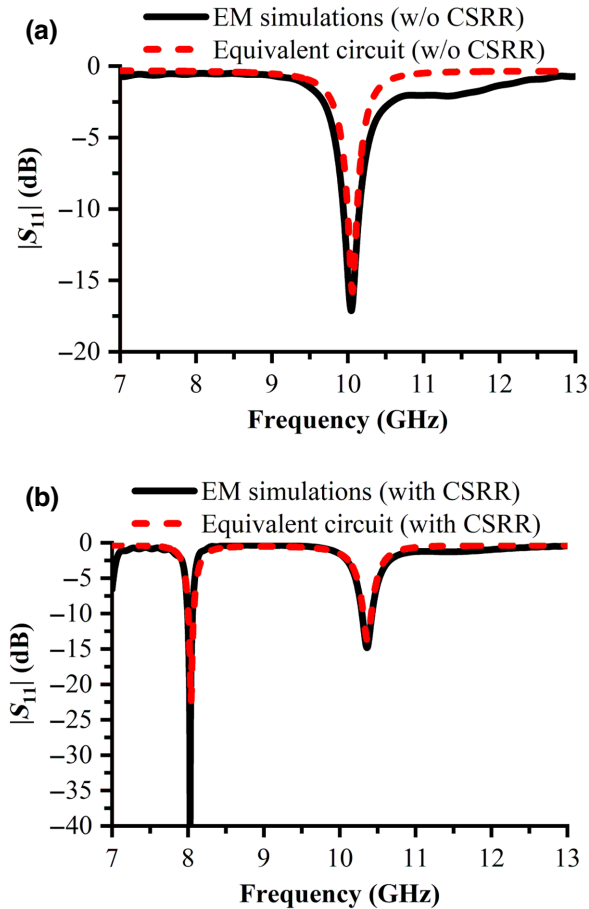


FIG. 6. EM and circuit simulations of the patch antenna (a) without and (b) with the back CSRR, in terms of  $|S_{11}|$  (dB).

## B. Ferroelectric-related tunability of the patch antenna integrated with a CSRR

In this section we present briefly how to implement an effective yet simple method to provide tunability characteristics to the patch antenna described before. In a way similar to Refs. [50,51], we designed and simulated a planar phase shifter in CPW technology, in order to emphasize the ferroelectric effect (in terms of both amplitude and phase) on the EM field propagating inside the structure and further radiated by the antenna. This phase shifter was created on the same HZO/HRSi substrate as the patch and is based on an interdigitated capacitor (IDC), onto which an external in-plane dc bias voltage  $V_b$  can be applied to change  $\epsilon_r^{\text{HZO}}$  (or, better,  $\epsilon_{\text{eff}}^{\text{HZO}}$ ). This choice was motivated by (i) the isotropic response of HZO under the application of an external electric field and (ii) the simplicity of the biasing technique in CPW technology, in which the dc voltage is applied onto the signal line and the lateral ground planes are set to 0 V (see Fig. 1). If we define with  $\beta_{\text{eff}}$  the effective phase constant of the IDC,  $L_{\text{IDC}}$  the length of the IDC, and  $f$  the frequency, then

$$\beta_{\text{eff}} L_{\text{IDC}} = \frac{2\pi f}{v_0} \sqrt{\epsilon_{\text{eff}}^{\text{HZO}}} L_{\text{IDC}}. \quad (5)$$

Hence, it is straightforward that tuning  $\epsilon_{\text{eff}}^{\text{HZO}}$  allows changing the phase between the input and output of the phase shifter. This phase shift can be used profitably to provide a further degree of freedom to the antenna integrated with the CSRR, in the sense of changing the resonant frequency, the matching properties, and the radiated power. The biggest advantage in using HZO is that it requires very small values of  $V_b$  (i.e., not exceeding  $\pm 5$  V) thanks to its nanoscale thickness, with excellent properties of resistance to external agents, time degradation, and temperature up to  $140^\circ$ .

The EM design of the phase shifter is shown in Figs. 7(a)–7(b), where  $C_{\text{SC}}$  is the short-circuit capacitor (SMD component to be soldered after fabrication),  $L_{\text{IDC}} = 102 \mu\text{m}$ , and  $W_{\text{IDC}} = 148 \mu\text{m}$ . The IDC is made of 30 digits and it can be modeled as a series  $R - L - C_{\text{IDC}}$  circuit, with  $R \in [10, 35] \Omega$ ,  $L = 20 \text{ pH}$ , and  $C_{\text{IDC}} \in [0.2, 1] \text{ pF}$ . The values for  $R$  and  $C_{\text{IDC}}$  are realistic, as they were extracted from previous experiments on similar structures. Figure 7(c) depicts the integration of the patch with the phase shifter (the substrate has been made transparent to

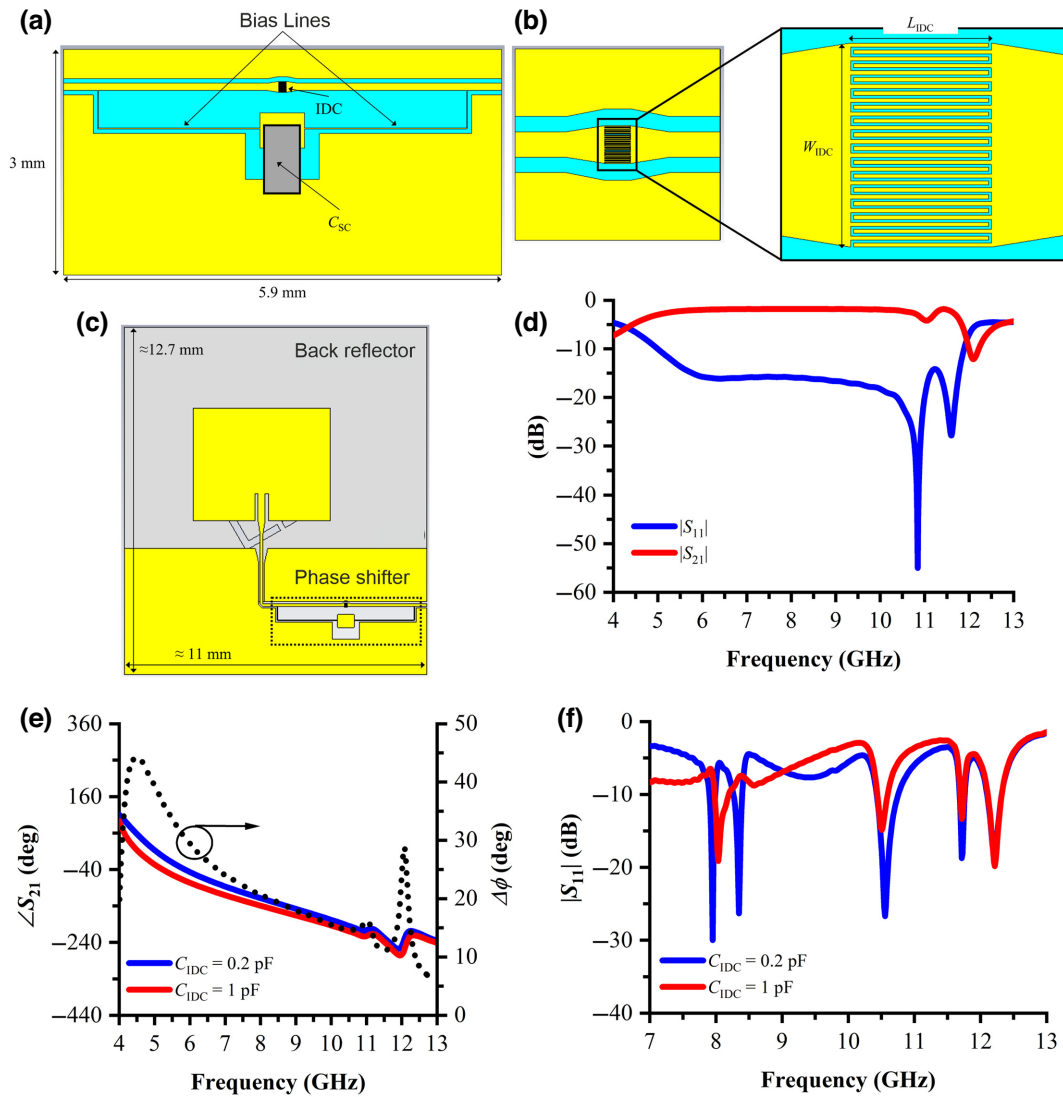


FIG. 7. EM design of the phase shifter: (a) top view and (b) detail of the IDC; (c) EM design of the patch antenna integrated with the phase shifter; EM simulations of the phase shifter (for  $R = 35 \Omega$ ): (d)  $|S_{11}|$  (dB) and  $|S_{21}|$  (dB); (e) unwrapped  $\angle S_{21}$ ; (f)  $|S_{11}|$  (dB) for the complete antenna and phase shifter at different values of  $C_{IDC}$ .

show the top and back metallization at the same time). From Fig. 7(d), one can see that the transmission coefficient  $|S_{21}|$  is very good in both the  $C$  (i.e., 4–8 GHz) and  $X$  band, attaining values between  $-2$  and  $-4$  dB, whereas  $|S_{11}|$  is always better than  $-10$  dB. Figure 7(e) shows on the left vertical axis the unwrapped results for  $\angle S_{21}$  at the minimum and maximum values of  $C_{IDC}$ , whereas the right vertical axis reports the total phase shift  $\Delta\phi$ , which is between  $10^\circ$  and  $29^\circ$  in the operating band of the patch antenna. Finally, Fig. 7(f) offers the overview of the reflection coefficient of the complete system made of phase shifter and antenna: the tuning effect coming from the HZO ferroelectric is visible in the position and amplitude of the resonant modes, corresponding to the two minima of  $|S_{11}|$  up to 11 GHz. The presence of the phase shifter

causes a pronounced shift of the first resonance but without affecting its radiation characteristics.

## IV. FABRICATION AND EXPERIMENTS

### A. Fabrication

For the fabrication of the patch antennas, the phase shifters, and the final prototypes, first we deposited an ultrathin layer of HZO directly on a 4-in. HRSi wafer by thermal atomic layer deposition (ALD). The process was the same as described in the Appendix of Ref. [40], followed by x-ray diffractivity (XRR) and grazing incidence x-ray diffraction (GIXRD) characterization. We report here only the hysteresis polarization-electric field  $P-E$  loop [see Fig. 8(a)], based on the Sawyer-Tower



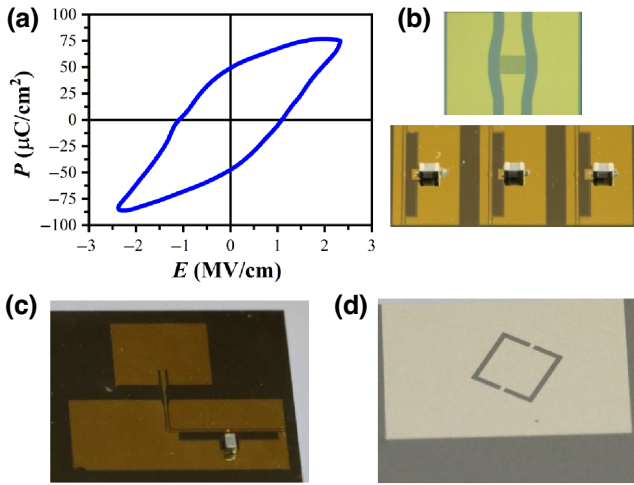


FIG. 8. (a) Experimental  $P - E$  loop of the HZO ultrathin film; optical pictures of (b) the phase shifters (up, the single IDC; down, the complete component) and (c) the final prototype integrating the patch antenna and the phase shifter; (d) optical image of the back reflector with the etched CSRR.

method [52,53]. The as-deposited HZO exhibits state-of-the-art values of coercive field  $E_c = 1.09$  MV/cm, remanent polarization  $P_r = 49.19$   $\mu\text{C}/\text{cm}^2$ , and spontaneous polarization  $P_s = 65.56$   $\mu\text{C}/\text{cm}^2$ , with excellent resistance to temperatures up to  $140^\circ\text{C}$  and very stable in time. The stabilization of a ferroelectric paracrystalline phase by oxygen vacancies engineering during the thermal ALD growth, together with the avoidance of a wake-up thermal treatment as in the case of the TiN/HZO/TiN approach, allow a great flexibility to be achieved for electronic devices and components working in the microwave and millimeter-wave bands.

The structure manufacturing had as main limitation the process temperature, that should not exceed  $120\text{--}130^\circ\text{C}$  due to the HZO, which loses its ferroelectric properties if the Curie temperature  $T_c$  is reached. The fabrication involved two metallization processes, one for each side of the wafer. On the front side (where the AUTs are patterned), the deposited metals were Ti (20 nm, for adhesion to HZO)/Au (230 nm); on the back (reflector) side, a 250-nm-thick layer of Al was used. In both cases, the metallization was patterned using a lift-off process with positive photoresist (AZ series 5200 from Clariant). The fabricated structures are displayed in Figs. 8(b)–8(d), in which the 0402 SMD capacitors  $C_{sc}$  are mounted as well.

## B. Experiments

The rf measurements of the patch antennas and of the standalone HZO-based phase shifters were performed using a vector network analyzer (VNA). In the case of the antenna, one port was connected to the AUT using standard CPW probe tips with pitch (distance between the

central line and the lateral ground) of  $150$   $\mu\text{m}$ , whereas the other port was connected to a standard 15-dBi-gain  $X$  band horn antenna fixed on a rigid nonmetallic arm. The AUT, the horn antenna, and the arm were inserted into a home-made anechoic chamber, internally covered with microwave absorber panels (Cuming Microwave C-RAM FAC-1.5  $24 \times 24''$  w/Velcro) to limit potential interferences and multipath effects, and suitable for far-field characterizations up to 40 GHz [Fig. 9(a)]. We measured the reflection ( $|S_{11}|$  and  $|S_{22}|$ ) and transmission ( $|S_{21}|$  and  $|S_{12}|$ ), which are identical because of the reciprocal characteristics of the system) coefficients of the standalone AUT. The AUT was put on a ROHACELL®HF layer (thickness of 15 mm) placed on the wooden surface of the anechoic chamber, and the CPW port of each AUT was contacted. Due to the stringent requirements of the experimental setup, we simulated again the antenna, this time with the actual materials under the back reflector (even if an ideal model was used for the wood under the ROHACELL layer). Of course, this entailed some unavoidable approximations, which lead to differences in the resonant frequency as it can be seen in Fig. 9(b). Nevertheless, the agreement between simulated and experimental data is good, proving the dual-band operation of the antenna. Next, in Figs. 9(c) and 9(d) we show the power transmitted by the AUT in the two bands of interest (and normalized with respect to the maximum value), i.e., around 8 and 10.5 GHz, respectively. In the first band, corresponding to the mode excited by the CSRR, the frequency downshift comes from the strong influence of the materials under the CSRR, as the latter is an aperture in the back reflector. On the other side, the radiation of the fundamental mode is, as expected, insensitive to the materials in contact with the CSRR. Then, in Fig. 9(e) we present the measured  $\Delta\phi$  and figure of merit [FOM, expressed in  $^\circ/\text{dB}$ , is defined as  $\text{FOM} = \Delta\phi/\text{IL}(0)$ , where  $\text{IL}(0)$  is the insertion loss of the phase shifter at 0 V]: the experimental phase shift is in good agreement with the results of Fig. 7(e), and FOM is between 1 and  $14^\circ/\text{dB}$ , a remarkable outcome considering the nanoscale nature of the HZO thin film.

In Figs. 10(a) and 10(b) we present the EM simulations of the reflection coefficient and of the normalized power pattern, respectively, for the final system made of the patch antenna with back CSRR and the HZO-based phase shifter, as a function of frequency and at different values of  $C_{\text{IDC}}$ . The simulations were performed using both a ROHACELL layer and a wooden surface. The tuning effect is evident in terms of resonant frequency, impedance matching, and gain when varying  $C_{\text{IDC}}$  (whose values were estimated from the measurements of the standalone phase shifter). In particular, from Fig. 10(b) one can see that the radiated power (hence, the gain) changes with several dB in correspondence of the resonance induced by the back CSRR, while the variation is less pronounced for the resonant mode.

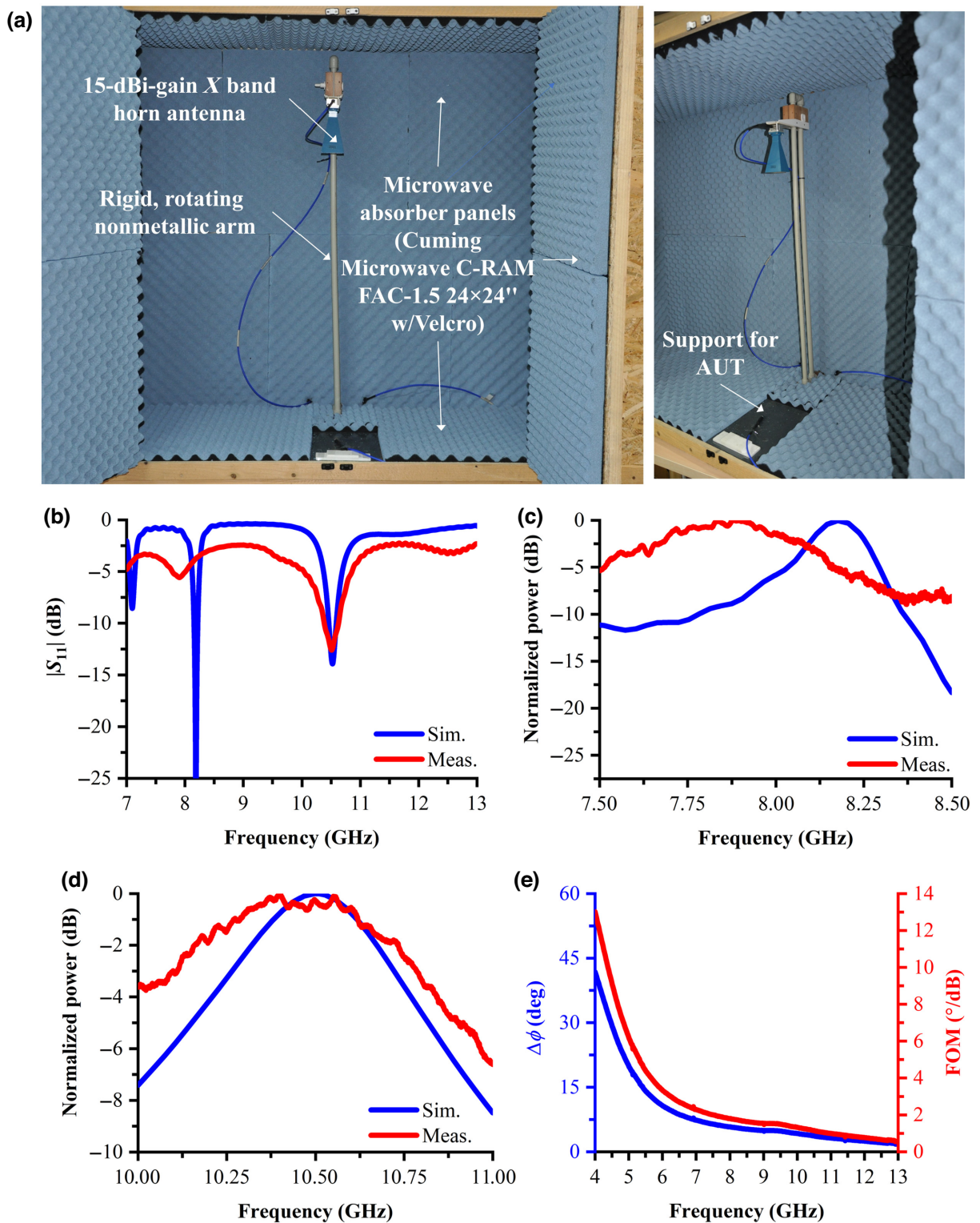


FIG. 9. (a) Microwave setup for far-field measurements. Comparison between simulations and measurements for the standalone antenna: (b)  $|S_{11}|$ ; far field in terms of normalized power (c) around 8 GHz and (d) around 10.5 GHz. (e) Measured  $\Delta\phi$  (left vertical axis, solid blue line) and FOM (right vertical axis, solid red line) for the standalone HZO-based phase shifter.

Finally, Fig. 10(c) displays the measured reflection coefficient of the antenna integrated with the phase shifter, in order to fully exploit the tunability offered by the HZO thin

film. One can notice that another resonance appears around 9 GHz, which was expected considering that the fabricated phase shifter has a maximum of impedance matching

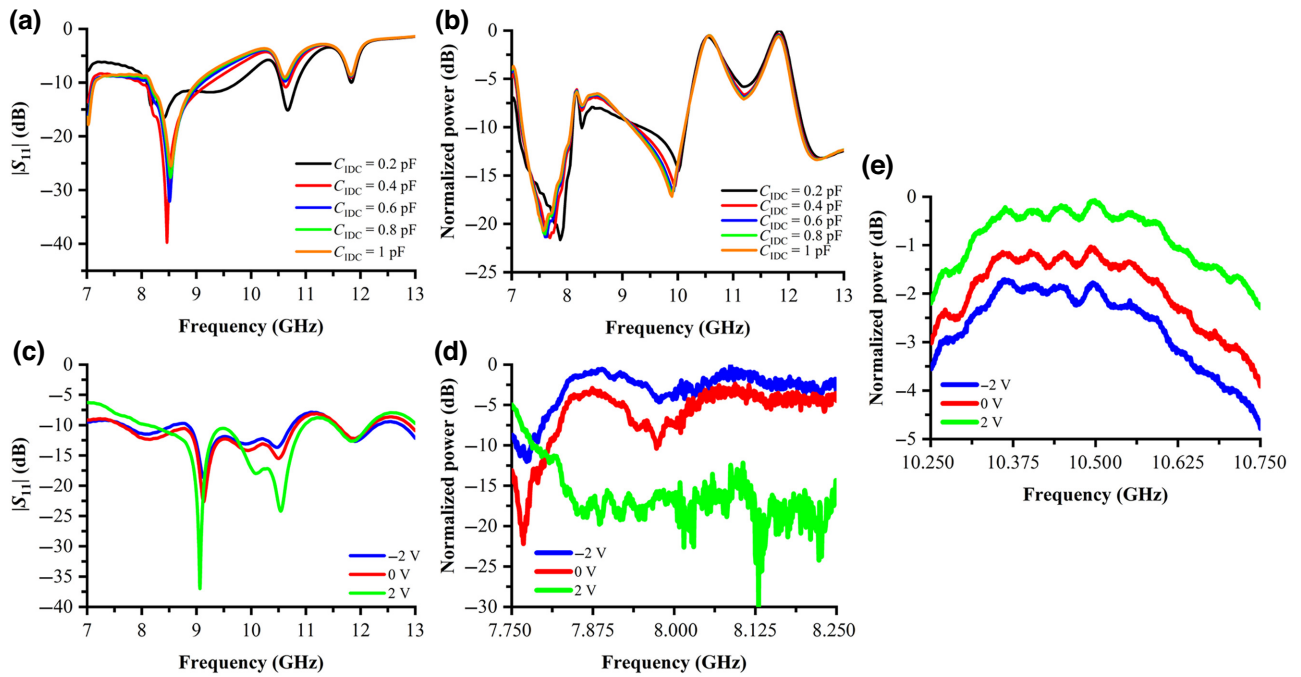


FIG. 10. Simulated (a)  $|S_{11}|$  and (b) far-field in terms of normalized power, as a function of frequency and at different values of  $C_{IDC}$ . Measured reflection coefficient and radiation characteristics of the fabricated prototypes, as a function of frequency and of the applied dc bias voltage: (c)  $|S_{11}|$ ; far field in terms of normalized power (d) around 8 GHz and (e) around 10.5 GHz.

(corresponding to a minimum of  $|S_{11}|$ ) around the same frequency. However, the two local minima of  $|S_{11}|$  around 8 and 10.5 GHz are still visible. The most useful results are the amplitude and frequency shifts of all the minima of  $|S_{11}|$  when applying a very low dc bias voltage between  $-2$  and  $2$  V. This outcome is in good agreement with the simulations displayed in Fig. 10(a), and is directly linked to the behavior of the AUT (in terms of radiated power) as a function of the bias in the two considered bands. For example, at 8 GHz we can modulate the power transmitted by the antenna (hence, the gain) with 16 dB

[Fig. 10(d)], whereas at 10.5 GHz the power modulation is greater than 2 dB [Fig. 10(e)]. Interestingly, the strongest effect can be observed on the radiating mode generated by the CSRR etched on the back metal reflector (even if  $|S_{11}|$  still exhibits a good value of  $-10$  dB at 8 GHz), meaning that the integration of metamaterials and nanoscale ferroelectrics is most efficient and does not hinder the matching and radiation characteristics of the fundamental mode. The same phenomenon is apparent in Fig. 10(b) but, with respect to the simulations, the measurements exhibit a more evident influence of the dc biasing. A possible

TABLE III. Comparison between different ferroelectric-based microwave antenna implementations.

Reference	Frequency (GHz)	Gain (dBi)	Multiband	Voltage range	Features
[54]	12–18	7	No	0–10 V	Patch antenna with frequency reconfigurability
[55]	9.9–14.2	5	No	0–10 V	Microstrip antenna with wideband frequency reconfigurability
[56]	1.3–2.4	7	Yes	0–10 V	U-slot dual-band frequency reconfigurable antenna
[57]	4–6	1.61	No	*magnetic bias	Patch antenna with frequency hybrid reconfigurability mediated by magnetic field
[58]	0.6–0.75	<sup>a</sup>	No	0–30 V	Notch miniaturized antenna with frequency reconfigurability
This work	8–12	4	Yes	$\pm 2$ V	Metamaterial enables dual-band functionality, whereas ferroelectric allows gain and frequency reconfigurability

<sup>a</sup>The gain is not provided, the demonstrated efficiency is up to 8%.

explanation is the powerful coupling between the CSRR and the HZO-loaded CPW line, not fully quantifiable from the EM simulations that need a huge memory occupation due to the high aspect ratio (between the minimum and maximum dimensions) coming from the thin ferroelectric layer. This aspect enhances the global varactor-type behavior of the phase shifter, thus leading to a strengthening of the tuning characteristics.

We stress that, unlike what happens at the fundamental resonance, negative and positive bias voltage values do not provide a monotone change in the radiated power, i.e., the macroscopic effect of the interaction between the CSRR and the ferroelectric layer is a loss of symmetry in the HZO thin film in relation with the mode excited by the CSRR itself.

Table III summarizes some typical design and experimental implementations involving ferroelectric-based antennas with different reconfigurable characteristics. As observed, the typical voltage range required for (mostly) frequency reconfigurability is equal or greater than 10 V, whereas in our case,  $\pm 2$  V are sufficient to provide for the desired tunable dual-band operation in terms of both frequency and gain.

## V. CONCLUSION

In this paper, we have presented the rigorous modeling, electromagnetic simulation, fabrication, and experimental validation of a dual-band patch antenna operating in the

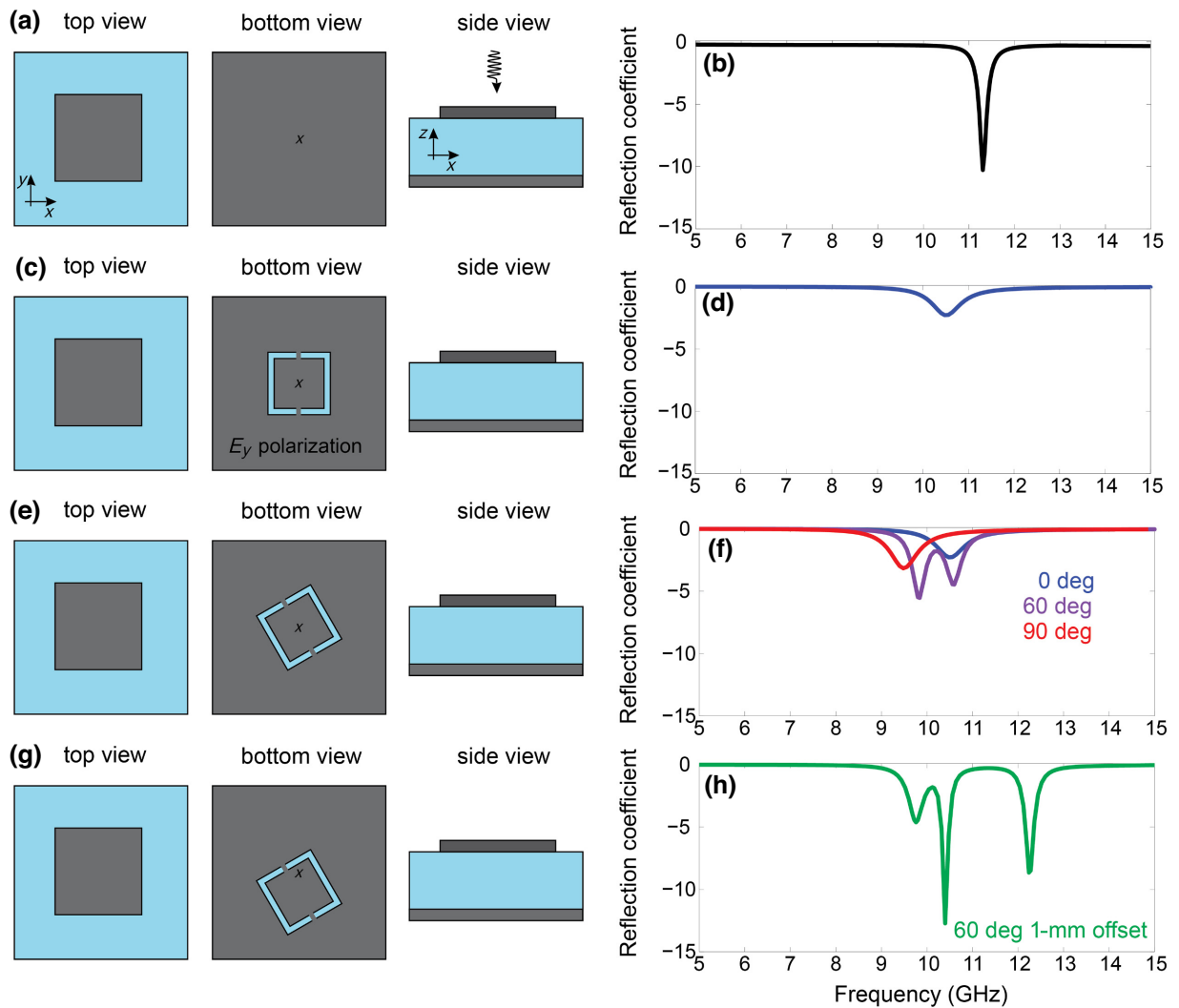


FIG. 11. Reflection coefficient spectra of the cavity for different cases and values of CSRR's rotation angle and offset, under the assumption of  $E_y$  polarization: (a) reflection spectrum for the single square patch atom with the uniform back reflector; (b) reflection spectrum for the square patch atom with the CSRR imprinted in the back reflector without rotation; (c) reflection spectrum for the square patch atom with the CSRR imprinted in the back reflector for three different rotation angles, i.e.,  $0^\circ$  (blue curve),  $60^\circ$  (purple curve), and  $90^\circ$  (red curve); (d) reflection spectrum for the square patch atom with the CSRR imprinted in the back reflector for a rotation angle of  $60^\circ$  and with a vertical offset.

$X$  band, integrated with a complementary split-ring resonator etched in the back reflector and with tunability characteristics coming from the presence of a nanometer-thick hafnium oxide-based ferroelectric layer. There are a very few attempts to efficiently integrate metamaterials with nanoscale ferroelectrics for very low-voltage microwave antennas. We have demonstrated that the application of a dc bias voltage of just  $\pm 2$  V allows tuning the matching and radiation performance of the antenna for the two modes excited by the rotation and asymmetric position of the back CSRR, with a sub- $\mu$ s response time, high repeatability of the results, and endurance in time as provided by the thin ferroelectric layer. Moreover, the technological process is CMOS compatible and requires a minimal number of well-developed steps. The proposed antenna represents a promising starting point toward the further progress in the domain of metamaterial-based antennas with improved functionalities for the actual and future technological challenges, in which a multidisciplinary approach will be mandatory to fully exploit the alternative upcoming materials.

### ACKNOWLEDGMENTS

This work was supported in part by a grant of the Romanian Ministry of Research, Innovation and Digitization, CCCDI-UEFISCDI, Project PN-III-P4-PCE-2021-0223, within PNCDI III, in part by the Core Program within the National Research Development and Innovation Plan 2022-2027, carried out with the support of MCID, Project No. 2307, in part by the European Project Horizon Europe HORIZON-EIC-2022-TRANSITIONCHALLENGES-01 “SMARTWAY” under Grant No. 101103057, and in part by the Foundation for Research and Technology Hellas (FORTH) under the Synergy Grant WISAR.

### APPENDIX A: CAVITY RESONANCE MODES

In this appendix, first we investigate in depth the cavity resonance modes. We assume a single cavity where a plane wave with linear polarization impinges normally onto the structure as it is shown in the schematics of Fig. 11. We focus on the  $E_y$ , since it is the dominant polarization of the patch antenna as we discuss later on. To facilitate the calculations, at the vertical sides of the structure we assume periodic conditions; however, the periodicity is large enough so that the neighbor coupling is minimal. We initially investigate the uniform metal-patch cavity seen in Fig. 11(a). The first schematic in Fig. 11(a) shows a top view of the cavity  $[(x, y)$  plane, where the metallic patch is depicted in gray and the dielectric layer in blue], the second shows the bottom view where we find the uniform metallic ground, and the third schematic shows a  $(x, z)$ -plane side view where we see the normally impinging wave. We assume  $E_y$  polarization (in the first case, i.e.,

without the CSRR, thanks to the symmetry the response is the same for both polarizations). The spectral response of the corresponding cavity is shown in Fig. 11(b). The cavity perfectly reflects the incoming wave apart from the area around the fundamental resonant frequency, at about 11.2 GHz, where a minimum dip in the reflection is experienced indicating that the cavity is matched with the free space and that the incoming energy is fully absorbed in the cavity mode.

The next step is to investigate the cavity’s response in the presence of the CSRR imprinted in the uniform back reflector. The corresponding structure is schematically shown in Fig. 11(c), top view of the patch, bottom view of the back reflector with the CSRR imprinted, and side view. The spectral response of the corresponding cavity is shown in Fig. 11(d). In comparison with the conventional patch cavity of Fig. 11(b), we observe a small shift to lower frequencies as a result of the back-reflector-induced resonance. The interesting response comes from the rotation of the CSRR resonator [Fig. 11(e)], the impact of which is shown in Fig. 11(f). Here we plot the reflection spectra of the cavity for three rotation angles, i.e.,  $0^\circ$  in blue,  $90^\circ$  in red, and  $60^\circ$  in purple. The  $90^\circ$  rotation results in a significant resonance shift toward lower frequencies in accordance to the meta-atom response shown in Fig. 2(b). Interestingly, as seen in Fig. 11(f) for the  $60^\circ$  rotation angle, we observe the presence of both the resonances in a partially merged form. Moreover, the merging of these two resonances leads to overall lower reflection dips, which point to a better impedance match for the corresponding antenna. The second source of the multimode response is the asymmetric displacement of the back-reflector CSRR, shown in Figs. 11(g) and 11(h). The vertical offset produces an additional reflection dip appearing at higher frequencies. These two asymmetries,

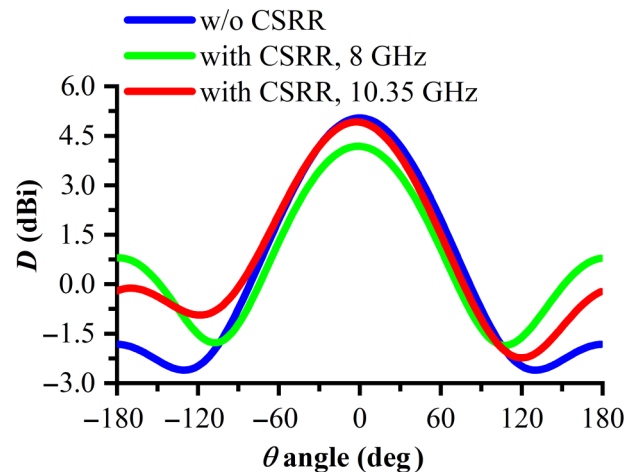


FIG. 12. EM simulations of the patch antenna without and with the back CSRR, in terms of directivity  $D$  (dBi).

i.e., the asymmetric rotation and the asymmetric relative plane positioning of the patch and of the CSRR lead to the multimode response and the deepening of the resonances that we use for the design of the patch antenna.

**APPENDIX B: DIRECTIVITY**

Figure 12 displays the directivity  $D$  without CSRR (at 10 GHz) and with CSRR (at 8 and 10.35 GHz).  $D$  is defined as follows [39]:

$$D = \frac{4\pi U}{P_{\text{rad}}}, \quad (\text{B1})$$

where  $U$  is the radiation intensity (in W/unit solid angle). Here, it is worth mentioning that the value of  $D$  for the dominant mode of the patch (i.e., around 10 GHz) is not affected by the multimode response in a wide  $\theta$ -angular

range, i.e.,  $[-70^\circ, 70^\circ]$ , where the angle  $\theta$  is defined in the  $(x, z)$  plane. In particular,  $D$  attains values between 1 and 5 dBi, with a side lobe level (SLL) of  $-6.9$  dB (antenna without CSRR),  $-3.4$  dB (antenna with CSRR, first resonance at 8 GHz), and  $-5$  dB (antenna with CSRR, second resonance at 10.35 GHz). Hence, the effect of the side lobes is stronger due to the multimode response; however, the values of SLL are always better than  $-3$  dB, meaning that the power radiated in the broadside direction (i.e., along the  $z$  axis, perpendicular to the  $(x, y)$  plane of the AUT) is always more than double with respect to the undesired side-lobe (back) radiation.

To prove that the EM effect of the CSRR etched on the back metallization is to provide an artificially increased value of  $\epsilon_{\text{eff}}$ , thus generating the alternative resonance at 8 GHz and basically preserving the dominant mode, we show here the EM simulated directivity in the  $(\theta, \phi)$

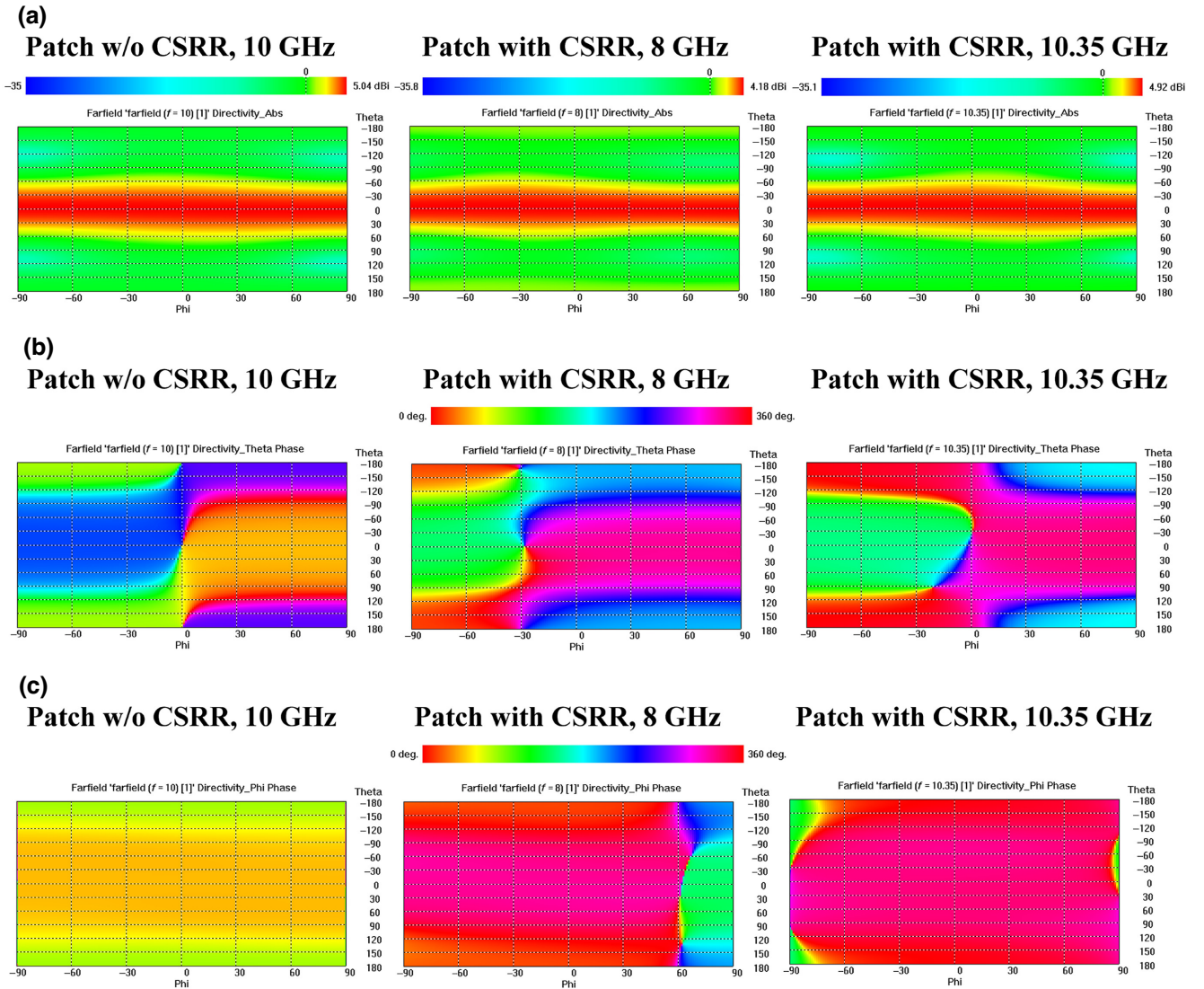


FIG. 13. EM simulations of the patch antenna without and with the back CSRR, in terms of (a)  $|D|$ , (b)  $D_\theta$ , and (c)  $D_\phi$ .

plane, in terms of absolute value  $|D|$  [Fig. 13(a)],  $\theta$ -phase  $D_\theta$  [Fig. 13(b)], and  $\phi$ -phase  $D_\phi$  [Fig. 13(c)]. In particular, Fig. 13(a) demonstrates that  $|D|$  is always in the broadside direction in the  $(y, z)$  plane; however, if we analyze  $D_\theta$  and  $D_\phi$ , the polarization effect due to the rotated CSRR is evident, with the two modes at 8 and 10.35 GHz having approximately the same 2D phase distribution.

**APPENDIX C: C-BAND SIMULATIONS**

From Fig. 6(b) it is evident that the EM simulations provide one more resonant mode at 7 GHz. In this section, we will try to give an explanation for the appearance of this extra resonance. In Fig. 14(a)–14(b) we show the EM simulations of the reflection coefficient and of the normalized power pattern, respectively, for the whole system, as a function of frequency and at different values of  $C_{IDC}$ , in the

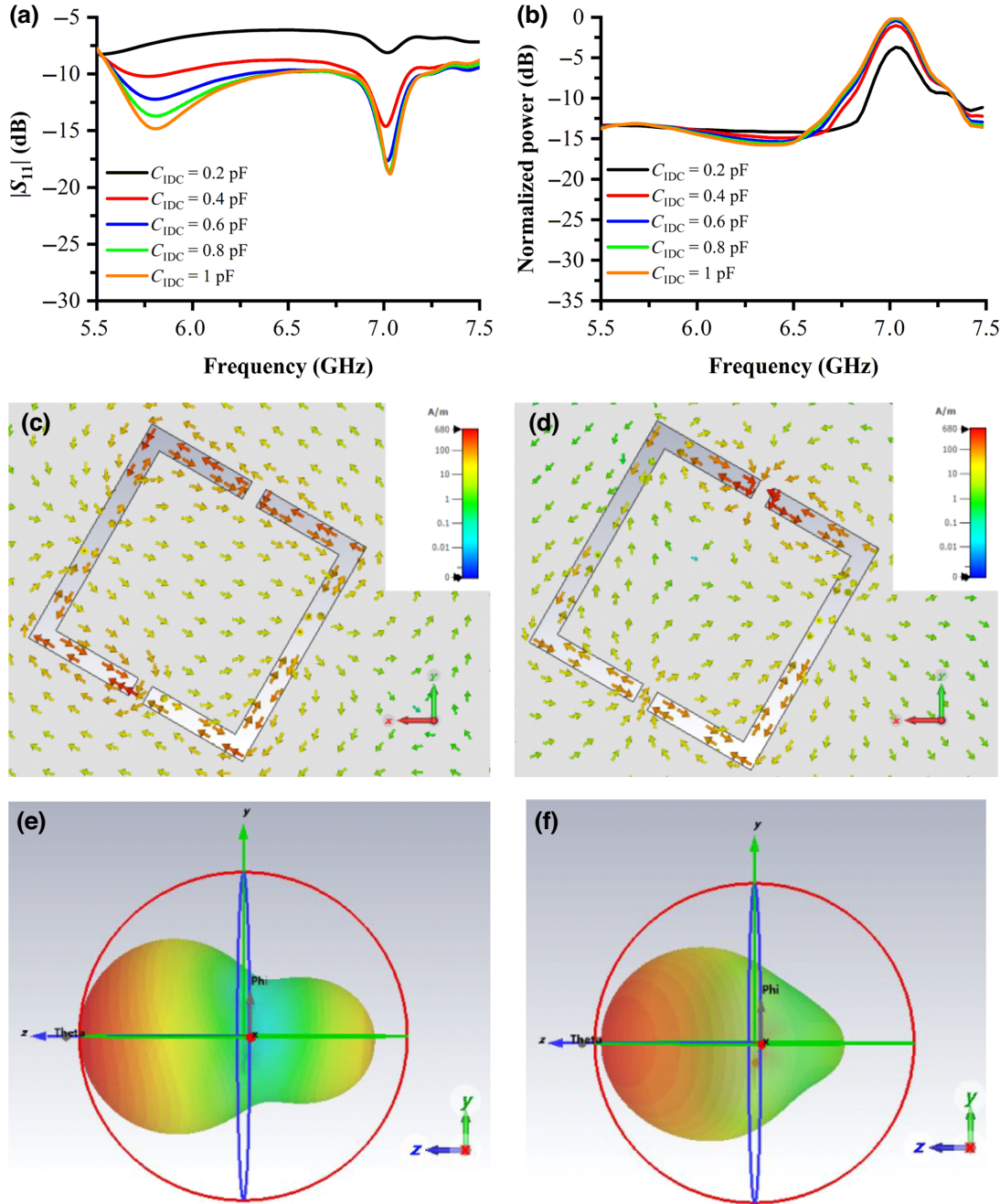


FIG. 14. Simulated (a)  $|S_{11}|$  and (b) far field in terms of normalized power, as a function of frequency and at different values of  $C_{IDC}$ , in the band 5.5–7.5 GHz; simulated surface currents at (c) 7 GHz and (d) 8 GHz; simulated far field at (e) 7 GHz and (f) 8 GHz in the  $(y, z)$  plane.

band 5.5–7.5 GHz. The tuning effect is still evident even at these frequencies (which fall within the *C* band, i.e., 4–8 GHz, where the gain of the horn antenna is undefined) and, what is more, the gain undergoes a 4-dB modulation at around 7 GHz. There is an intrinsic difference with respect to the resonant modes in the *X* band, which are coming from the coupling between the patch antenna and the CSRR. In fact, Fig. 14(c) shows the surface currents at the edges of the CSRR at 7 GHz, in comparison with the surface currents at 8 GHz [Fig. 14(d)]. In the first case, the direction of the currents suggests a dipolelike behavior, more specifically a half-wavelength dipolelike one: indeed, the half-perimeter length of the CSRR coincides with the length of a half-wavelength dipole on HRSi substrate and resonating around 7.2 GHz [exactly where the maximum radiation occurs, see Fig. 14(b)]. A further proof of this explanation comes from the simulated far field at 7 GHz [Fig. 14(e)] in comparison with the radiation pattern at 8 GHz [Fig. 14(f)]: at 7 GHz there is a pronounced backside radiation, with a side-lobe level of just  $-1.3$  dB, whereas at 8 GHz the radiation is clearly broadside, with a side-lobe level of  $-4.5$  dB. Hence, we can conclude that at 7 GHz we observe the radiation of the CSRR as if it were a standalone half-wavelength dipole on HRSi, with an efficiency smaller than that at 8 GHz but potentially useful for a triple-band operation of the patch antenna integrated with the back CSRR. From the point of view of the equivalent circuit, the schematic in Fig. 6(b) would necessitate one more *RLC* resonator to model the dipolelike resonance.

- 
- [1] Y. Dong and T. Itoh, Metamaterial-based antennas, *Proc. IEEE* **100**, 2271 (2012).
- [2] S. B. Glybovski, S. A. Tretyakov, P. A. Belov, Y. S. Kivshar, and C. R. Simovski, Metasurfaces: From microwaves to visible, *Phys. Rep.* **634**, 1 (2016).
- [3] M. Chen, M. Kim, A. M. Wong, and G. V. Eleftheriades, Huygens' metasurfaces from microwaves to optics: A review, *Nanophotonics* **7**, 1207 (2018).
- [4] M. Wang, D. Liao, J. Y. Dai, and C. H. Chan, Dual-polarized reconfigurable metasurface for multifunctional control of electromagnetic waves, *IEEE Trans. Antennas Propag.* **70**, 4539 (2022).
- [5] A. D. Koulouklidis, A. C. Tasolamprou, S. Doukas, E. Kyriakou, M. S. Ergoktas, C. Daskalaki, E. N. Economou, C. Kocabas, E. Lidorikis, M. Kafesaki, and S. Tzortzakis, Ultrafast terahertz self-induced absorption and phase modulation on a graphene-based thin film absorber, *ACS Photonics* **9**, 3075 (2022).
- [6] Q. He, S. Sun, and L. Zhou, Tunable/reconfigurable metasurfaces: Physics and applications, *Research* **2019**, 27 (2019).
- [7] T. A. Tsiftsis, C. Valagiannopoulos, H. Liu, A.-A. A. Boulogeorgos, and N. I. Miridakis, Metasurface-coated devices: A new paradigm for energy-efficient and secure 6g communications, *IEEE Veh. Technol. Mag.* **17**, 27 (2022).
- [8] C. Liaskos, A. Tsioliariidou, K. Georgopoulos, I. Morianos, S. Ioannidis, I. Salem, D. Manassis, S. Schmid, D. Tyrovolas, S. A. Tegos, P.-V. Mekikis, P. D. Diamantoulakis, A. Ptilakis, N. V. Kantartzis, G. K. Karagiannidis, A. Tasilamprou, O. Tsilipakos, M. Kafesaki, I. F. Akyildiz, A. Pitsillides, M. Pateraki, M. Vakalellis, and I. Spais, Xr-rf imaging enabled by software-defined metasurfaces and machine learning: Foundational vision, technologies and challenges, *IEEE Access* **10**, 119841 (2022).
- [9] M. Di Renzo, F. H. Danufane, and S. Tretyakov, Communication models for reconfigurable intelligent surfaces: From surface electromagnetics to wireless networks optimization, *Proc. IEEE* **110**, 1164 (2022).
- [10] P. Kumar, T. Ali, and M. M. M. Pai, Electromagnetic metamaterials: A new paradigm of antenna design, *IEEE Access* **9**, 18722 (2021).
- [11] L.-Y. Liu and B.-Z. Wang, A broadband and electrically small planar monopole employing metamaterial transmission line, *IEEE Antennas Wirel. Propag. Lett.* **14**, 1018 (2015).
- [12] R. Alaei, M. Albooyeh, S. Tretyakov, and C. Rockstuhl, Phase-change material-based nanoantennas with tunable radiation patterns, *Opt. Lett.* **41**, 4099 (2016).
- [13] Y. He, N. Ding, L. Zhang, W. Zhang, and B. Du, Short-length and high-aperture-efficiency horn antenna using low-loss bulk anisotropic metamaterial, *IEEE Antennas Wirel. Propag. Lett.* **14**, 1642 (2015).
- [14] S. A. Amanatiadis, T. D. Karamanos, and N. V. Kantartzis, Radiation efficiency enhancement of graphene THz antennas utilizing metamaterial substrates, *IEEE Antennas Wirel. Propag. Lett.* **16**, 2054 (2017).
- [15] X. Yang, Y. Liu, Y.-X. Xu, and S. X. Gong, Isolation enhancement in patch antenna array with fractal UC-EBG structure and cross slot, *IEEE Antennas Wirel. Propag. Lett.* **16**, 2175 (2017).
- [16] Z. L. Ma, C. H. Chan, K. B. Ng, and L. J. Jiang, in *Proc. of 2017 IEEE International Symposium on Antennas and Propagation & USNC/URSI National Radio Science Meeting* (IEEE, San Diego, CA, USA, 2017).
- [17] Y. A. Kamel, H. A. Mohamed, H. ELsadek, and H. M. ELhennawy, Miniaturized triple-band circular polarized implantable patch antenna for bio-telemetry applications, *IEEE Antennas Wirel. Propag. Lett.* **22**, 74 (2022).
- [18] R. S. Malfajani, F. B. Ashraf, and M. S. Sharawi, A 5G enabled shared-aperture, dual-band, in-rim antenna system for wireless handsets, *IEEE Open J. Antennas Propag.* **3**, 1013 (2022).
- [19] H. Tang, C. J. Bulger, T. Rovere, B. Zheng, S. An, H. Li, Y. Dong, M. Haerinia, C. Fowler, S. Gonya, W. Guo, and H. Zhang, A low-profile flexible dual-band antenna with quasi-isotropic radiation patterns for MIMO system on UAVs, *IEEE Antennas Wirel. Propag. Lett.* **22**, 49 (2022).
- [20] G. Yang and S. Zhang, Dual-band shared-aperture multiple antenna system with beam steering for 5G applications, *IEEE Trans. Circuits Syst. II Express Briefs* **69**, 4804 (2022).
- [21] A. A. Ka'bi, in *Proc. of 2022 IEEE International Black Sea Conference on Communications and Networking (Black-SeaCom)* (IEEE, Sofia, Bulgaria, 2022).



- [22] M. Ramzan and P. Sen, in *Proc. of 2022 Joint European Conference on Networks and Communications & 6G Summit (EuCNC/6G Summit)* (IEEE, Grenoble, France, 2022).
- [23] C. Sahana, D. M. Nirmala, and M. Jayakumar, in *Proc. of 2022 IEEE Region 10 Symposium (TENSYMP)* (IEEE, Mumbai, India, 2022).
- [24] H. U. Tahseen, R. Colella, F. P. Chietera, L. Yang, and L. Catarinucci, in *Proc. of 2022 7th International Conference on Smart and Sustainable Technologies (SpliTech)* (IEEE, Split/Bol, Croatia, 2022).
- [25] H. Badgajar, A. Khan, F. Carvalho, A. Kotrashetti, S. Ghosh, and S. Bhattacharyya, in *Proc. of 2022 IEEE Region 10 Symposium (TENSYMP)* (IEEE, Mumbai, India, 2022).
- [26] V. G. Ataloglou, G. Egorov, J. Kim, G. Xu, A. H. Dorrah, A. Ohadi, M. Kim, and G. V. Eleftheriades, Static and reconfigurable Huygens' metasurfaces: Use in antenna beamforming and beam steering, *IEEE Antennas and Propag. Mag.* **64**, 73 (2022).
- [27] S. Poddar, A. M. Holmes, and G. W. Hanson, Design and analysis of an electronically tunable magnet-free non-reciprocal metamaterial, *IEEE Trans. Antennas Propag.* **70**, 7311 (2022).
- [28] S. K. Ghosh, S. Das, and S. Bhattacharyya, Graphene-based metasurface for tunable absorption and transmission characteristics in the near mid-infrared region, *IEEE Trans. Antennas Propag.* **70**, 4600 (2022).
- [29] H. Taghvaei, A. Ptilakis, O. Tsilipakos, A. C. Tasolamprou, N. V. Kantartzis, M. Kafesaki, A. Cabellos-Aparicio, E. Alarcón, and S. Abadal, Multiwideband terahertz communications via tunable graphene-based metasurfaces in 6G networks: Graphene enables ultimate multiwideband THz wavefront control, *IEEE Veh. Technol. Mag.* **17**, 16 (2022).
- [30] A. E. Gayduk and S. V. Golod, in *Proc. of 2022 IEEE 23rd International Conference of Young Professionals in Electron Devices and Materials (EDM)* (IEEE, Altai, Russian Federation, 2022).
- [31] Y. Che, X. Wang, Q. Song, Y. Zhu, and S. Xiao, Tunable optical metasurfaces enabled by multiple modulation mechanisms, *Nanophotonics* **9**, 4407 (2020).
- [32] N. Katsarakis, M. Kafesaki, I. Tsiapa, E. N. Economou, and C. M. Soukoulis, High transmittance left-handed materials involving symmetric split-ring resonators, *Photonics Nanostruct.: Fundam. Appl.* **5**, 149 (2007).
- [33] A. C. Tasolamprou, D. Mentzaki, Z. Viskadourakis, E. N. Economou, M. Kafesaki, and G. Kenanakis, Flexible 3D printed conductive metamaterial units for electromagnetic applications in microwaves, *Materials* **13**, 3879 (2020).
- [34] F. Monticone and A. Alù, The quest for optical magnetism: from split-ring resonators to plasmonic nanoparticles and nanoclusters, *J. Mater. Chem. C* **2**, 9059 (2014).
- [35] I. Katsantonis, M. Manousidaki, A. D. Koulouklidis, C. Daskalaki, I. Spanos, C. Kerantzopoulos, A. C. Tasolamprou, C. M. Soukoulis, E. N. Economou, S. Tzortzakos, M. Farsari, and M. Kafesaki, Strong and broadband pure optical activity in 3D printed THz chiral metamaterials, *Adv. Opt. Mater.* **11**, 2300238 (2023).
- [36] A. Bitzer, A. Ortner, H. Merbold, T. Feurer, and M. Walther, Terahertz near-field microscopy of complementary planar metamaterials: Babinet's principle, *Opt. Express* **19**, 2537 (2011).
- [37] T. Zentgraf, T. P. Meyrath, A. Seidel, S. Kaiser, H. Giessen, C. Rockstuhl, and F. Lederer, Babinet's principle for optical frequency metamaterials and nanoantennas, *Phys. Rev. B* **76**, 033407 (2007).
- [38] L. Zhang, T. Koschny, and C. M. Soukoulis, Creating double negative index materials using the Babinet principle with one metasurface, *Phys. Rev. B* **87**, 045101 (2013).
- [39] C. A. Balanis, *Antenna Theory: Analysis and Design* (Wiley, 2016), 4th ed.
- [40] M. Aldrigo, M. Dragoman, S. Iordanescu, F. Nastase, S. Vulpe, A. Dinescu, and D. Vasilache, Low-voltage permittivity control of coplanar lines based on hafnium oxide ferroelectrics grown on silicon, *IEEE Access* **7**, 136686 (2019).
- [41] R. Placeres-Jiménez, J. P. Rino, and J. A. Eiras, Modeling ferroelectric permittivity dependence on electric field and estimation of the intrinsic and extrinsic contributions, *J. Phys. D: Appl. Phys.* **48**, 035304 (2015).
- [42] M. Narayanan, S. Tong, B. Ma, S. Liu, and U. Balachandran, Modified Johnson model for ferroelectric lead lanthanum zirconate titanate at very high fields and below curie temperature, *Appl. Phys. Lett.* **100**, 022907 (2012).
- [43] T. Prakoso, R. Ngah, Z. Ghassemlooy, and T. A. Rahman, Antenna representation in two-port network scattering parameter, *Microw. Opt.* **53**, 1404 (2011).
- [44] J. B. Coder, J. M. Ladbury, and M. Gołkowski, A two-port model for antennas in a reverberation chamber, *IEEE Trans. Antennas Propag.* **62**, 2338 (2014).
- [45] P. Groves, P. Conroy, L. Belostotski, and M. Okoniewski, in *Proc. of 2016 10th European Conference on Antennas and Propagation (EuCAP)* (IEEE, Davos, Switzerland, 2016).
- [46] P. Groves, P. Conroy, L. Belostotski, and M. Okoniewski, Antenna 2-port electrical and noise parameters, *IEEE Antennas Wirel. Propag. Lett.* **16**, 1265 (2016).
- [47] P. L. Tokarsky, A. A. Konovalenko, and S. N. Yerin, Sensitivity of an active antenna array element for the low frequency radio telescope GURT, *IEEE Trans. Antennas Propag.* **65**, 4636 (2017).
- [48] P. L. Tokarsky, Antenna analytical representation by a two-port network, *Int. J. Antennas Propag.* **2020**, 2609747 (2020).
- [49] Z. Xu, J. Shi, R. J. Davis, X. Yin, and D. F. Sievenpiper, Rainbow trapping with long oscillation lifetimes in gradient magnetoinductive metasurfaces, *Phys. Rev. Appl.* **12**, 024043 (2019).
- [50] M. Dragoman, M. Modreanu, I. Povey, S. Iordanescu, M. Aldrigo, A. Dinescu, D. Vasilache, and C. Romanitan, 2.55 GHz miniaturised phased antenna array based on 7 nm-thick  $Hf_xZr_{1-x}O_2$  ferroelectrics, *Electron. Lett.* **54**, 469 (2018).
- [51] M. Dragoman, M. Aldrigo, S. Iordanescu, M. Modreanu, I. Povey, D. Vasilache, A. Dinescu, and C. Romanitan, in

- Proc. of the 48th European Microwave Conference (EuMC)* (IEEE, Madrid, Spain, 2018).
- [52] C. B. Sawyer and C. H. Tower, Rochelle salt as a dielectric, *Phys. Rev.* **35**, 269 (1930).
- [53] M. Dragoman, M. Aldrigo, D. Dragoman, S. Iordanescu, A. Dinescu, S. Vulpe, and M. Modreanu, Ferroelectrics at the nanoscale: Materials and devices—A critical review, *Crit. Rev. Solid State Mater. Sci.* **48**, 561 (2022).
- [54] Y. Wang, Y. Liu, H. Du, C. Liu, Q. Xue, X. Gao, S. Li, and Y. Lu, A frequency reconfigurable microstrip antenna based on (Ba, Sr)TiO<sub>3</sub> substrate, *IEEE Trans. Antennas Propag.* **63**, 770 (2015).
- [55] Y. Wang, C. Liu, B. Sun, Y. Liu, X. Sun, F. Li, and Y. Lu, Design of an instantaneous-wideband frequency reconfigurable microstrip antenna based on (Ba, Sr)TiO<sub>3</sub>/MgO composite thin films, *IEEE Trans. Antennas Propag.* **62**, 6472 (2014).
- [56] M. V. Carballo, D. Borah, and T. S. Kalkur, in *2019 IEEE International Conference on Microwaves, Antennas, Communications and Electronic Systems (COMCAS)* (IEEE, Tel-Aviv, Israel, 2019), p. 1.
- [57] Q. Lou, R.-X. Wu, F.-G. Meng, and Y. Poo, Realizing frequency reconfigurable antenna by ferrite-loaded half-mode SIW, *Microw. Opt. Technol. Lett.* **59**, 1365 (2017).
- [58] H. V. Nguyen, R. Benzerga, C. Borderon, C. Delaveaud, A. Sharaiha, R. Renoud, C. L. Paven, S. Pavy, K. Nadaud, and H. W. Gundel, Miniaturized and reconfigurable notch antenna based on a BST ferroelectric thin film, *Mater. Res. Bull.* **67**, 255 (2015).